Journal of
Materials Chemistry C

PAPER

View Article Online
View Journal | View Issue

Cite this: *J. Mater. Chem. C*, 2025, **13**, 17838

# Fast, slow and reverse polymorph transformations in thin films of a 5,10-dihydroindolo[3,2-*b*]indole derivative†

Niklas J. Herrmann,[a] Oleksandra Korychenska,[b] Ngoc Phi Ta,[a] Guy E. Mayneord,[c] Xabier Rodríguez-Martínez,[ad] Daniel T. W. Toolan,[e] Craig C. Robertson,[b] Ahmed Iraqi,[b] Jenny Clark *[b] and Jana Zaumseil *[a]

Received 14th May 2025,
Accepted 24th July 2025

DOI: 10.1039/d5tc01928a

rsc.li/materials-c

Many small-molecule organic semiconductors can crystallize in different polymorphs, which influences their electronic (charge transport) and optical (absorption and fluorescence) properties. Understanding polymorph formation and transformation is crucial to control these properties for potential applications. Here we explore different thin films of a newly synthesized derivative of 5,10-dihydroindolo[3,2-*b*]indole, which shows high photoluminescence quantum yields even in the solid state as well as hole transport. Deposition of this indoloindole-based p-type semiconductor by thermal evaporation and zone-casting from solution results in distinct film morphologies and a metastable polymorph that can transform into more stable polymorphs at room temperature over timescales from hours to months. Their conversion and changing structural, optical and electronic properties are characterized by grazing incidence wide-angle X-ray scattering (GIWAXS), atomic force microscopy (AFM), absorption, fluorescence, and Raman spectroscopy as well as charge transport measurements in field-effect transistors (FET). Rough and polycrystalline films result in very fast polymorph transformation, while defect-free and smooth zone-cast films are stable for several months. Annealing these films does not lead to faster conversion but instead to thermodynamic stabilisation of the metastable polymorph and thus even a reversal of aged thin films. For this and potentially other organic polymorphic systems, long-term retention of a metastable polymorph and its electronic and optical properties can be achieved by controlling the initial film morphology, while annealing can indeed induce the formation of metastable polymorphs.

## 1. Introduction

Many small organic molecules can form several different stable or metastable crystal structures, that is, they exhibit polymorphism.[1] For organic semiconductors (OSCs), the orbital overlap and electronic coupling between the molecules can strongly vary between different polymorphs giving rise to substantially different electrical and optical properties that impact their applicability in optoelectronic devices.[2–9] Different polymorphs are usually identified by single-crystal X-ray structure analysis[10,11] or grazing incidence wide-angle X-ray scattering (GIWAXS) for thin films.[3,12–15] Furthermore, low-frequency Raman spectroscopy,[4,16,17] and even fluorescence spectra[18] can reveal the presence of different polymorphs.

The formation of a specific polymorph can be controlled by the type of film deposition or crystal growth methods (*e.g.*, physical vapor transport, thermal evaporation, or solution processing) and their specific conditions.[19,20] However, the initially formed polymorphs are often not the most thermodynamically stable polymorph,[21] allowing for polymorph transformations and potential device degradation to take place over time. Long-term stability or transformation into other metastable or stable polymorphs depend on intrinsic as well as extrinsic factors. Intrinsic factors are, for example, the intermolecular interaction strength and film morphology, while temperature, humidity, and the presence of additional compounds (*e.g.*, solvent vapours) are important external parameters.[3,10,20,22–25] These parameters mainly affect the kinetic barriers to molecular reorientation and/

---

[a] *Institute for Physical Chemistry, Heidelberg University, 69120 Heidelberg, Germany. E-mail: zaumseil@pci.uni-heidelberg.de*
[b] *School of Mathematical and Physical Sciences, Hounsfield Road, Sheffield S3 7RH, UK. E-mail: jenny.clark@sheffield.ac.uk*
[c] *School of Biosciences, University of Sheffield, Firth Court, Western Bank, Sheffield, S10 2TN, UK*
[d] *Universidade da Coruña, Centro de Investigación en Tecnoloxías Navais e Industriais (CITENI), Campus de Esteiro, 15403 Ferrol, Spain*
[e] *Department of Materials, The University of Manchester, Engineering Building A, Booth Street East, Manchester M13 9PL, UK*

† Electronic supplementary information (ESI) available. CCDC 2448535 and 2448536. For ESI and crystallographic data in CIF or other electronic format see DOI: **https://doi.org/10.1039/d5tc01928a**

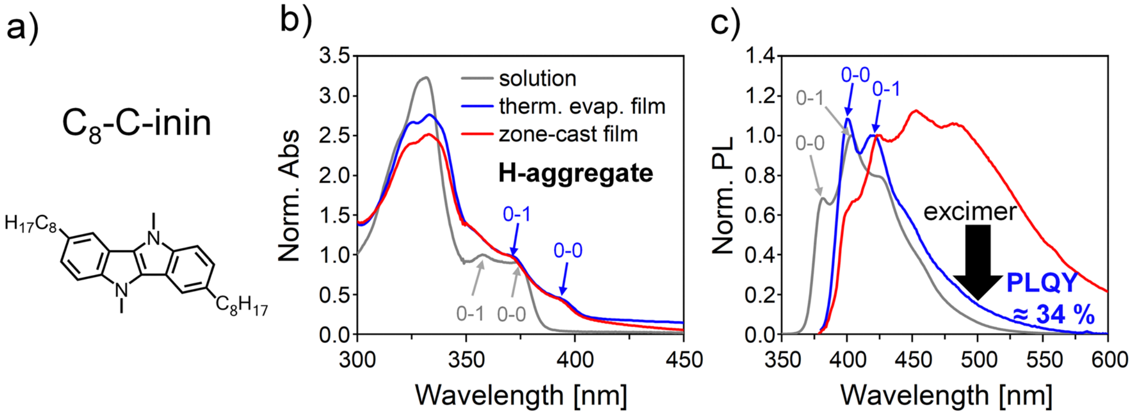

Fig. 1 (a) Molecular structure of $C_8$-C-inin. Normalized (b) absorption and (c) photoluminescence (PL) spectra of $C_8$-C-inin in hexane solution (grey), of thermally evaporated (blue) and zone-cast (red) thin films.

or the relative thermodynamic stability (*i.e.*, Gibbs free energy) of the different polymorphs.[14] The latter determines the thermodynamic driving force behind polymorph transformations.

Here we investigate the polymorph transformations of a newly synthesized derivative of 5,10-dihydroindolo[3,2-*b*]indole (ININ, also known as dibenzopyrolo[3,2-*b*]pyrrole) with methylated nitrogen atoms and an octyl chain at each of the benzene rings (3,8-dioctyl-5,10-dimethylindolo[3,2-*b*]indole; $C_8$-C-inin, see Fig. 1a). $C_8$-C-inin can be viewed as nitrogen-substituted near-analogue of the benchmark p-type organic semiconductor $C_8$-BTBT.[26] ININ derivatives possess an electron-rich and rigid planar core structure,[27] which has led to their use as p-type semiconductors in organic field-effect transistors (OFETs)[28,29] and as donor molecules in solar cells (both as small molecules and donor–acceptor copolymers).[30–34] In addition, many ININ derivatives have high photoluminescence quantum yields (PLQYs), even in the solid state, and can be functionalized to exhibit thermally activated delayed fluorescence (TADF).[35,36] Consequently, ININ-based materials have been used for high-efficiency organic light-emitting diodes (OLEDs).[35,37,38] The small molecular core and easy functionalization with additional side-chains enable thin film deposition *via* thermal evaporation as well as solution-based methods. This versatility of film formation and functionalization also facilitates variations of morphology and molecular packing over a wide range.[29] However, unlike the sulfur-substituted analogues of ININs (such as BTBTs: benzothieno[3,2-*b*]benzothiophene),[13,24,39] and despite the intriguing properties of the ININ class molecules, their polymorphism and its impact on optoelectronic properties have not yet been explored.

Here we employ thermal evaporation and zone-casting from solution to create thin films of $C_8$-C-inin with markedly different macro- and microscopic morphologies and study their influence on polymorph formation, transformation, and stability. By combining atomic force microscopy (AFM), GIWAXS, Raman and absorption/fluorescence spectroscopy we explore the different polymorphs and the molecular rearrangements during polymorph transformation. Variations in crystallinity and morphology directly affect the transformation kinetics (fast or slow) in different thin films as large molecular reorientations occur. Furthermore, we identify conditions for which polymorph transformation processes can be reversed.

## 2. Results and discussion

### 2.1. Optical properties of $C_8$-C-inin

The new ININ derivative $C_8$-C-inin (see molecular structure in Fig. 1a) was synthesised *via* a reductive ring closure approach adapted from Qiu *et al.* (see reaction scheme, synthesis details and analysis in ESI,† Fig. S1–S11).[40] Thermogravimetric analysis (TGA) shows that $C_8$-C-inin remains stable up to 220 °C with only 5% weight loss up to 300 °C (see ESI,† Fig. S12), thus enabling a broad temperature window for processing. Cyclic voltammetry of a 1 mM $C_8$-C-inin solution in degassed dichloromethane (see ESI,† Fig. S13) indicates two sequential oxidation steps. However, the second oxidation step is irreversible. The corresponding ionization potentials (IPs) relative to the vacuum level were extracted as $IP1 = -4.76$ eV and $IP2 = -5.44$ eV (see ESI,† Table S1). The first IP is sufficiently close to the work function of gold or silver to enable hole injection into $C_8$-C-inin in OFETs, although, the secondary irreversible oxidation process may limit device stability.

The absorption spectrum of $C_8$-C-inin in hexane solution (Fig. 1b) shows two main absorption bands that are common for ININ-derivatives and are associated with the $S_0 \rightarrow S_1$ (376 nm) and the $S_0 \rightarrow S_2$ (333.5 nm) transition.[40] Absorption and emission band positions were determined from the second derivatives of the smoothed spectra to correct for peak shifts due to band overlap. The $S_0 \rightarrow S_1$ transition shows a typical vibronic progression with the 0–0 band at 376 nm and the 0–1 band at 357.5 nm. The photoluminescence spectrum (Fig. 1c) mirrors the vibrational progression of the absorbance (0–0 band at 379 nm and 0–1 band at 403 nm). The relatively rigid molecular core structure is reflected in a small Stokes shift of only 3 nm. High photoluminescence quantum yields (PLQY) of 87 ± 11% were observed for deoxygenated toluene solutions of $C_8$-C-inin.

Thin films of $C_8$-C-inin were deposited in two different ways, by slow thermal evaporation (0.2 Å $s^{-1}$) in vacuum and by zone-casting from toluene solutions ($T_{stage}$ = 80 °C, $T_{solution}$ = 60 °C, casting speed 0.1 mm $s^{-1}$). Both types of films show nearly identical absorption spectra (see Fig. 1b) indicating very similar molecular packing orders. An additional peak not detectable in the solution spectrum appears at ~354 nm in the fresh thin-film spectra. Its exact identity remains uncertain, but it might correspond to the 0–2 peak, which is too weak to be observed for the isolated molecules in solution as it would be covered by the strong $S_0 \rightarrow S_2$ transition. For both thin films, the 0–0/0–1 band intensity ratio is lower than in the solution spectrum. This change in ratio indicates the formation of H-aggregates as a result of close molecular packing with direct overlap of the π-electron systems of the neighbouring molecules.[41] However, the observed redshift of the 0–0 (solution: 376 nm, therm. evap.: 395 nm, zone-cast: 394 nm) and 0–1 absorption bands (solution: 357.5 nm, therm. evap.: 373 nm, zone-cast: 372 nm) is in contrast to the expected blueshift for H-aggregates. Due to the rigidity of the molecular core (the π-electron system) we can rule out conformational changes in the solid state as the reason behind the changed vibronic coupling and the spectral redshift. However, this discrepancy might be attributed to a relatively small excitonic coupling, with the blueshift due to H-aggregation being smaller than the stabilization by dispersive forces in the solid state resulting in a 'solution-to-crystal' redshift. Similar behaviour has been observed for H-aggregates of other molecules.[41] Thermally evaporated $C_8$-C-inin films still showed fairly high PLQYs of 34 ± 4% despite H-aggregates usually leading to suppressed PL.[41] Some solid state emitters with vibrational coupling and low excitonic coupling have been shown to retain high PLQYs if the non-radiative decay rates are slow.[41–43] However, this is relatively rare for polycrystalline films, in contrast to single-crystals, as large numbers of grain boundaries often lead to fast non-radiative decay.

Zone-cast films of $C_8$-C-inin clearly show fewer grain boundaries, however, their PL spectra also differ substantially from the evaporated polycrystalline films. The PL spectrum (see Fig. 1c) shows a strong and broad emission band around 500 nm and a reduced 0–0/0–1 intensity ratio compared to the thermally evaporated film. The spectral evolution of the PL spectra of thermally evaporated $C_8$-C-inin films at 77 K from 0 to 10 ns and time-resolved PL decay measurements reveal a long-lived emission at 500 nm (see ESI,† Fig. S14). Together with its occurrence only in the solid state, we attribute this broad emission feature to excimer species that are more pronounced in the zone-cast films due to increased long-range order. The increased excimer intensity and its overlap with the 0–1 band but not the 0–0 band explains the smaller 0–0/0–1 PL band ratio of the zone-cast film compared to the thermally evaporated film despite their very similar 0–0/0–1 absorption band ratios.

## 2.2. Thin film morphology

The similar molecular packing of the evaporated and zone-cast films as indicated by their closely resembling absorption spectra but their differences in long-range order as implied by the

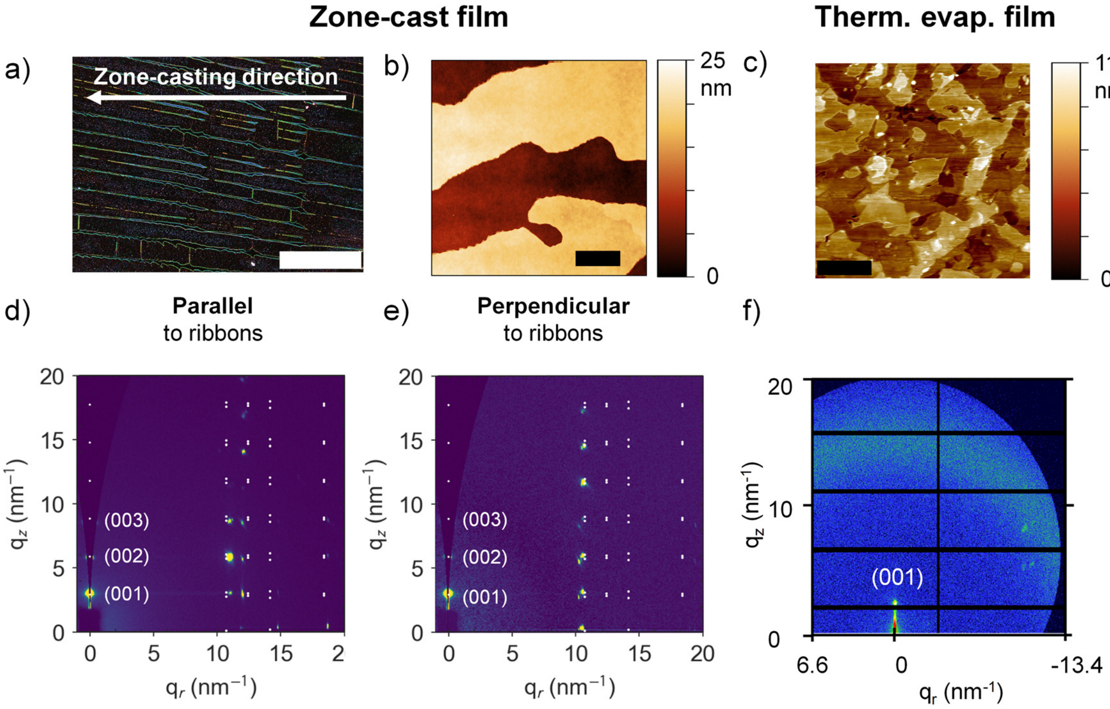

Fig. 2 (a) Darkfield optical micrograph (scale bar 200 μm) and (b) AFM image of zone-cast $C_8$-C-inin film (scale bar 1 μm). (c) AFM image of thermally evaporated thin film (scale bar 1 μm). GIWAXS data of zone-cast film with X-ray propagation direction (d) parallel and (e) perpendicular to crystalline ribbons. White dots (also included in the missing wedge) indicate diffraction peak positions calculated from unit cell parameters. The associated crystal planes are labelled by their Miller indices. (f) GIWAXS data of thermally evaporated $C_8$-C-inin film.

different excimer emission intensities are further visualized and confirmed by optical micrographs, AFM images, GIWAXS and X-ray diffraction (XRD) data as shown in Fig. 2. Zone-casting leads to highly aligned, millimetre-long, smooth crystalline ribbons (see Fig. 2a and b), while thermal evaporation yields polycrystalline films with a rough island-like morphology (see Fig. 2c). The excellent in-plane and out-of-plane order of the zone-cast films is highlighted by sharp GIWAXS reflections and their dependence on sample orientation (90° rotation, compare Fig. 2d and e). The unit cell parameters for the crystalline zone-cast ribbons were extracted from the GIWAXS data *via* iterative diffraction peak simulation and are listed in Table S2 (ESI†). An out-of-plane stacking distance of 2.2 nm (*c*-axis = 2.8 nm, $\beta$ = 127°) was further corroborated by a minimum step height of 2.1 ± 0.2 nm extracted from AFM images of the zone-cast films. With a total molecular length (molecular long axis, extended alkyl chains) of approximately 2.8 nm, the out-of-plane packing distance of 2.1–2.2 nm suggests that the molecules are standing upright but slightly tilted on the substrate surface. Such a molecular orientation was also observed for several other ININ derivatives.[29] While the thermally evaporated films did not show any long-range in-plane order in GIWAXS experiments (see Fig. 2f), their crystallinity and out-of-plane order are clearly represented by sharp XRD reflections (see ESI,† Fig. S15). The out-of-plane packing distance of 2.1 ± 0.1 nm of the thermally evaporated films suggests a local packing order that is very similar to the zone-cast films.

Large single-crystals of $C_8$-C-inin were grown from a THF:hexane solvent mixture (slow solvent diffusion) and also by recrystallization from toluene. The obtained single-crystal structures are different for crystals grown from the THF:hexane compared to crystals from toluene solution (see ESI,† Fig. S16–S19). However, both crystal types show nearly the same peaks in differential scanning calorimetry (DSC) (see ESI,† Fig. S20) with an endothermic peak on first heating at 103.5 °C/104.6 °C (potential polymorph transformation) and a second endothermic peak at 151.6 °C/152.6 °C (melting). We attribute the similarity of the DSC data for the two crystal types to their similar intermolecular interactions. The two bulk-phase single-crystal structures share an interlocking pattern of the octyl chains between layers and small overlaps between the π-electron systems of neighbouring molecules. Both single-crystal structures exhibit unit cell parameters that are different from those of the thin films (see ESI,† Table S3). A much larger *c*-axis length of 3.5–3.6 nm compared to the 2.8 nm of the thin films is most obvious. The smaller out-of-plane packing distance of the thin films excludes the possibility of interlocking octyl chains between layers. Overall, $C_8$-C-inin layers created by thermal evaporation and zone-casting yield a unique thin-film polymorph that is different from bulk single-crystals. The existence of multiple crystal structures poses the question of packing stability and the possibility of polymorph transformations.

### 2.3. Polymorph transformations

The occurrence of metastable polymorphs and their successive transformation into more stable polymorphs can lead to performance degradation of small-molecule thin-film optoelectronic devices. The optical and charge transport properties of different polymorphs often deviate substantially due to variations in their intermolecular interactions. Furthermore, degradation may occur due to changes in film morphology or volume during polymorph transformation, leading to cracks or adhesion issues at the interfaces between different layers (electrode-semiconductor or semiconductor–dielectric interface).[22,44] Hence, we analysed the

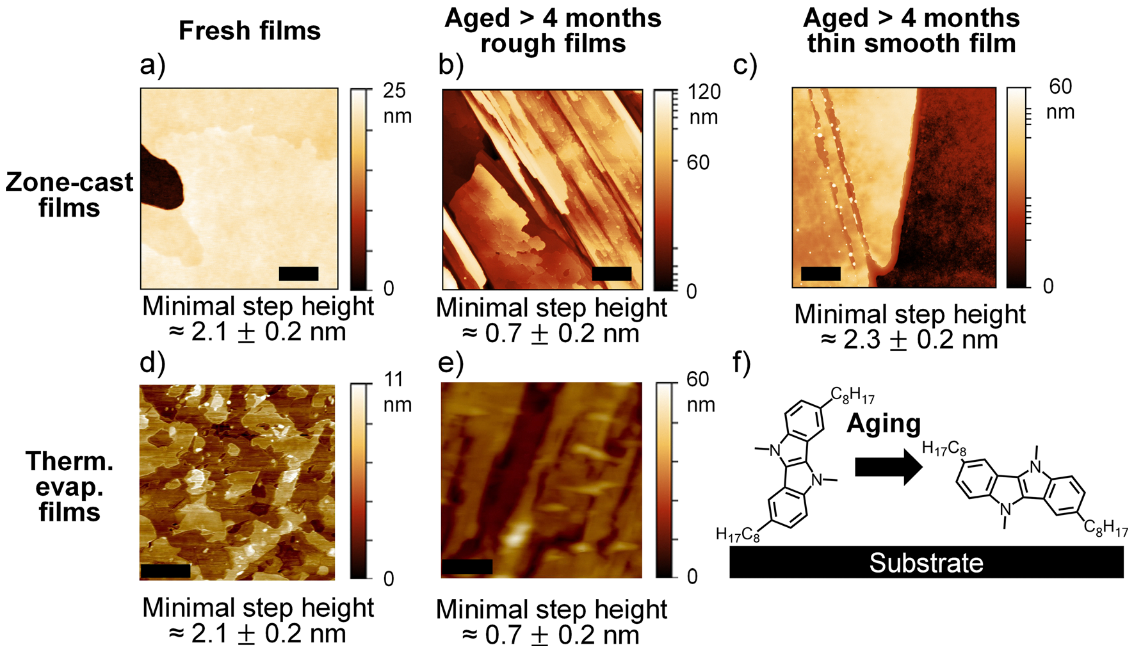

Fig. 3 AFM images (scale bar 1 μm) of (a)–(c) zone-cast and (d) and (e) thermally evaporated $C_8$-C-inin films, either freshly deposited or after storage in dry nitrogen for more than 4 months. (f) Schematic of the proposed molecular reorientation during the aging process.

stability of the $C_8$-C-inin thin-film polymorphs that were created by thermal evaporation and zone-casting from a few hours to several months.

For a polycrystalline thermally evaporated $C_8$-C-inin film, the first morphology changes occurred within a few hours after deposition (see ESI,† Fig. S21). Consecutive AFM images collected over 8 hours at room temperature (ESI,† Video S1) show significant diffusion of material and drastically changing surface topology. In contrast to that, zone-cast films only showed significant morphology changes after 1–2 months. Fig. 3 shows the morphology changes of the thermally evaporated and zone-cast films after more than 4 months of storage in dry nitrogen at room temperature. A clear transformation to needle-like layers and a strong reduction of the minimal step height from $2.1 \pm 0.2$ nm to $0.7 \pm 0.2$ nm occurred for most zone-cast films (Fig. 3a and b) and all of the thermally evaporated films (Fig. 3d and e). However, for a few zone-cast crystalline ribbons (Fig. 3c) with very smooth surfaces (homogeneous height, very low number of molecular steps, edges, and defects), no morphology or significant step height changes ($2.1 \pm 0.2$ nm to $2.3 \pm 0.2$ nm) were observed even after over 4 months. These different transformation kinetics for thermally evaporated films and zone-cast films of different roughness clearly indicate different kinetic barriers for the transformation in these films.

The decreased out-of-plane packing distance of the transformed films suggests that the $C_8$-C-inin molecules not only diffuse over the substrate but also tilt to a more parallel orientation to the substrate plane (see schematic of molecular orientations in Fig. 3f). GIWAXS data of the aged thermally evaporated films provide further evidence for the reorientation of the molecules (see ESI,† Fig. S22). They show sharp reflections instead of diffuse rings, thus indicating increased in-plane order. The unit cell parameters of the aged thermally evaporated film were extracted from GIWAXS data *via* iterative diffraction peak fitting and simulation (see ESI,† Table S4). These unit cell parameters differ from all other polymorphs that were discussed so far, thus indicating a polymorph transformation during film aging. The extracted out-of-plane distance of ∼0.7 nm corresponds well to the minimal AFM step height. The longest in-plane distance of ∼2.8 nm is in good agreement with a mostly parallel orientation of the molecular long axis relative to the substrate plane.

The aging/polymorph transformation processes of $C_8$-C-inin thin films are also reflected in their absorption and PL spectra. Fig. 4a and b show the corresponding spectra of a fresh and aged thermally evaporated film and bulk-phase single-crystals (recrystallized from hexane). The relative absorption band intensities changed significantly with aging while transition energies remained mostly the same with only a slight blueshift of 9 nm, indicating a modified intermolecular orientation but no chemical degradation. The 0–0/0–1 absorption band ratio is sensitive to changes in the intermolecular excitonic coupling, which in turn is related to changes in the molecular packing.[41] The similarity between the 0–0/0–1 absorption band ratios of the aged film and the single-crystal powder suggests a similar packing order in both. The 0–0/0–1 ratio is near unity and thus equal to the ratio observed for the molecules in solution (see Fig. 1b), suggesting very small intermolecular excitonic coupling in contrast to the small 0–0/0–1 ratio of the fresh films indicative of H-aggregates.

The main difference between the PL spectra of aged thermally evaporated film and the bulk-phase single-crystals (Fig. 4b) is the very low emission intensity at the 0–0 band for the single-crystals. This can be explained by the higher self-absorption of the latter caused by an increased optical path length due to the thickness of the crystallites as well as waveguiding. Both single-crystals and aged films show relatively low excimer emission intensities despite the clearly higher long-range order compared to the freshly thermally evaporated film. For single-crystals, this could be a consequence of the small overlap of the π–π-electron

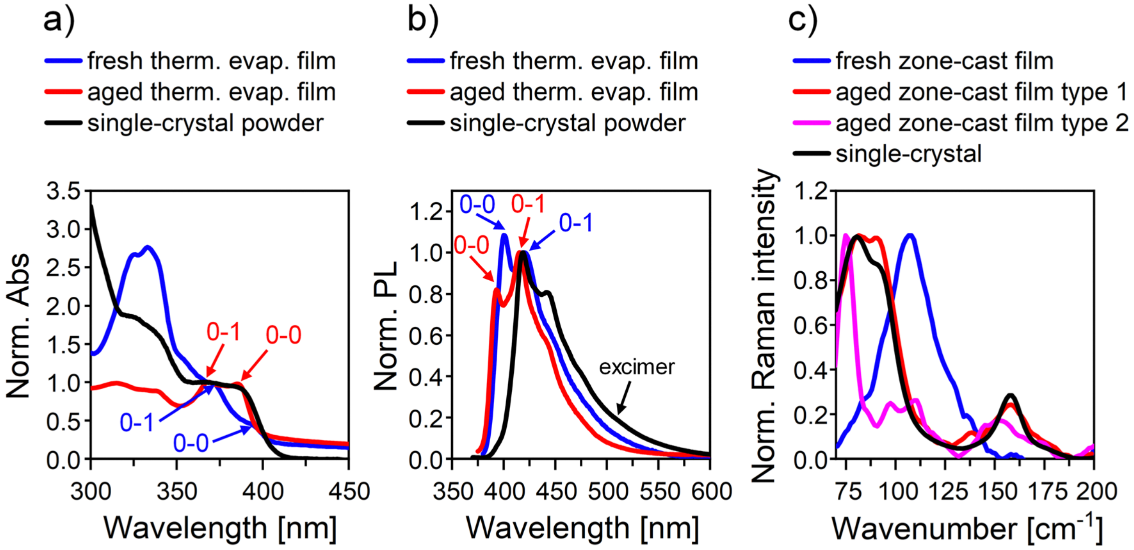

Fig. 4 Normalized (a) absorption and (b) PL spectra of fresh and aged (>4 months) thermally evaporated thin-film and of bulk-phase single-crystals. (c) Baseline-corrected normalized low-frequency Raman spectra of fresh and aged/transformed zone-cast films and bulk-phase single-crystals.

systems between neighbouring molecules (ESI,† Fig. S16–S19) and represents additional evidence for a similar molecular packing order in aged films.

To summarize, while the unit cell parameters of the polymorphs of the aged films and single-crystals are clearly different, the next-neighbour orientations and interactions appear to be quite similar for the two samples. Only the longest unit cell axes are significantly different (~2.8 nm *vs.* 3.5 nm) which might be explained by a slightly higher symmetry in the packing along these axes. Nearest neighbour interactions along these axes should only consist of interactions between octyl-chains. Hence, the intermolecular excitonic coupling along these axes is negligible due to the large distances between the molecular cores. They should have no significant influence on the absorption and emission properties. These observations explain the seemingly contradictory results of similar optical properties but different unit cell parameters of the aged thin film polymorph and the bulk-phase single-crystals.

To further explore the similarities and distinctions of the different molecular packing orders, we applied low-frequency Raman microscopy. As Raman modes below ~200 $\text{cm}^{-1}$ are mostly attributed to intermolecular vibrations and rotations they depend on the molecular packing and can be used to distinguish between different polymorphs.[4,16,17] Fig. 4c shows the low-frequency Raman spectra of a freshly zone-cast film of two different aged zone-cast films and of bulk-phase single-crystals. While the single-crystals showed Raman bands at 80, 90 and 158 $\text{cm}^{-1}$, the freshly zone-cast films exhibited one main band at 107 $\text{cm}^{-1}$ and smaller features at 87, 96, and 116 $\text{cm}^{-1}$, again indicating different polymorphs in agreement with AFM, GIWAXS, and absorption data. Aged zone-cast films exhibited two distinct types of Raman spectra (referred to as type 1 and type 2 in the following) associated with slightly different morphologies (ESI,† Fig. S23). Here, type 1 was the predominant form of aged zone-cast films and had a mostly needle-like morphology as already shown in Fig. 3b (see also ESI,† Fig. S23). This morphology is similar to that of aged evaporated films, suggesting that the type 1 polymorph observed in aged zone-cast films is probably the same as that of aged evaporated films. Type 1 films display Raman signals identical to those of single-crystal powder (80, 90 and 158 $\text{cm}^{-1}$), indicating similar intermolecular vibrations and rotations, thereby confirming the presence of the same or at least very similar polymorphs in the aged zone-cast film and the single-crystal powder.

In contrast to that, type 2 was only observed for a small minority of aged zone-cast $C_8$-C-inin ribbons and exhibited a more island-like surface morphology (ESI,† Fig. S23) but still a similar minimum step height of 0.7 ± 0.2 nm. Type 2 films feature a unique Raman signal at 75 $\text{cm}^{-1}$, alongside additional peaks with small relative intensities close to those observed in fresh zone-cast films (85, 97 and 110 $\text{cm}^{-1}$) and single-crystal powder (153 $\text{cm}^{-1}$). We postulate a co-existence of the fresh thin-film, the bulk-phase single-crystal-like, and a potential third polymorph in different areas of the type 2 films. This third polymorph may represent a transitional phase from the metastable thin-film polymorph to the stable bulk-phase single-crystal-like polymorph. Overall, low-frequency Raman spectroscopy can be used to identify and track different polymorph transformations of $C_8$-C-inin films by probing the whole volume of a measurement spot and not just the surface (as in AFM).

Interestingly, smooth zone-cast films did not show any morphology changes (AFM) or changes of the low-frequency Raman modes compared to the fresh zone-cast films even after nine months (ESI,† Fig. S24). Hence, we hypothesize that the differences in polymorph stability and the transformation speed of rough and smooth zone-cast films and thermally evaporated films are the result of a higher kinetic barrier for molecular diffusion and rotation/reorientation in closely packed crystalline ribbons. Molecular reorientation requires free volume, and such space would only be available at grain boundaries, crystal edges, and packing defects. At these positions, which are numerous in the polycrystalline thermally evaporated films and rougher zone-cast ribbons, the kinetic barrier should be low enough to permit polymorph transformation at room temperature.

We tested this hypothesis by observing the birefringence of different $C_8$-C-inin films with cross-polarized microscopy at different temperatures. The transformed polymorphs of aged thin films (both type 1 and type 2) were strongly birefringent but nearly no birefringence was observed for the metastable polymorph of freshly deposited films (see ESI,† Fig. S25a and b). Bright-field optical microscope images did not show enough contrast to locate areas with polymorph transformation (see ESI,† Fig. S25c and d). However, differences in birefringence allowed for tracking the polymorph transformations over much larger areas than AFM or Raman measurements.

Films consisting mainly of very smooth, low-defect ribbons were deposited by lowering the $C_8$-C-inin concentration of the toluene solutions used for zone-casting to 0.25 mg $\text{mL}^{-1}$ (compared to 2.5 mg $\text{mL}^{-1}$). The smooth zone-cast films showed no transformation of the metastable thin-film polymorph even after prolonged heating (up to 4 hours) at 60 °C, 80 °C, 110 °C, or 130 °C. Heating to 150–160 °C resulted in melting of the thin film (melting temperature of bulk-phase single-crystals ~152 °C). The stability observed at low temperatures (close to room temperature) might be attributed to a high kinetic barrier for polymorph transformation in highly ordered crystal ribbons. However, the absence of transformations at elevated temperatures, such as 130 °C, indicates the presence of another contributing factor. In addition to kinetics, thermodynamic aspects must also be considered.

Polymorphic systems exhibit a transformation temperature at which the relative thermodynamic stability (Gibbs free energy) of the polymorphs switch order (see schematic for a dimorphic system in Fig. 5a).[21] Hence, while the kinetic barrier of molecular reorientation in a system might be overcome at higher temperatures, the thermodynamic driving force for the transformation is lost. Consequently, no conversion from thin-film polymorph to bulk-phase or aged thin-film polymorph can occur. However, at temperatures above the transformation

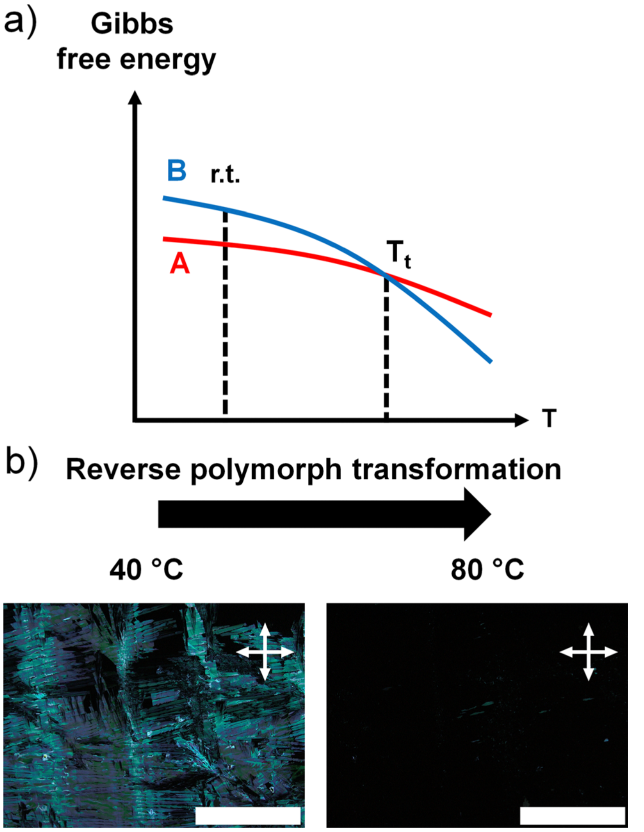

Fig. 5 (a) Schematic representation of the Gibbs free energy – temperature relationship of a dimorphic system (polymorphs A and B) with room temperature (r.t.) and transformation temperature ($T_t$) indicated with dashed lines. (b) Cross-polarized images (white crosses indicate relative orientation of polarization filters) of aged (transformed) zone-cast film before and after heating to 80 °C in steps of 10 °C for 10 min starting at 40 °C (scale bar 1 mm).

point the reverse process should occur, *i.e.*, conversion of the formerly thermodynamically stable polymorph into the metastable polymorph. The only additional conditions are that the transformation temperature must be lower than the melting temperature of both polymorphs (enantiotropic system)[23] and the kinetic barrier can be overcome.

To test for such a reverse polymorph transformation, an aged zone-cast $C_8$-C-inin film with clear birefringence was heated from 40 °C to 80 °C in steps of 10 °C for 10 min each. The birefringent polymorph remained stable up to 70 °C but around 80 °C a fast transformation towards the non-birefringent polymorph occurred (see Fig. 5b and ESI,† Fig. S26). AFM images show that the film surface changed from a needle-like morphology to an island-like morphology (see ESI,† Fig. S27). The minimum step-height of the film changed from 0.7 ± 0.2 nm to 2.1 ± 0.2 nm. In addition, the low-frequency Raman spectrum of the annealed film showed no significant differences to the spectra of freshly zone-cast films (see ESI,† Fig. S28). Thus, AFM and Raman data confirm that annealing indeed induced a reverse polymorph transformation back to the thin-film polymorph of freshly zone-cast $C_8$-C-inin films.

Cross-polarized microscope images during annealing of the aged zone-cast film show that the polymorph transformation occurred *via* a nucleation and growth mechanism (see Video S2 and Fig. S29, ESI†). Nucleation and growth transitions are the most common transition types and occur generally for polymorph transformations with significant changes in molecular packing, where molecules move individually across phase boundaries (in contrast to martensitic transitions).[3,45] Note, that all nucleation events occur at positions where lower kinetic barriers towards molecular reorientation can be expected (*i.e.*, crystal edges, grain boundaries). For nucleation and growth transitions, defects in molecular packing and grain boundaries increase the rate of polymorph transformation.[45–48]

Overall, these experiments support our hypothesis that the polymorph metastability of $C_8$-C-inin is strongly influenced by the film morphology, especially the presence or absence of grain boundaries and defects. They are the origin of the vastly different polymorph transformation kinetics in thermally evaporated films and different zone-cast films.

## 2.4. Charge transport properties

The ability to maintain the metastable thin film polymorph for certain crystalline ribbons but observe polymorph transformation for other film morphologies allows us to distinguish the impact of polymorph transformation on the charge transport properties of $C_8$-C-inin films from other processes that may occur during long-term storage. The close molecular packing and long-range order of the zone-cast films of $C_8$-C-inin as well as the ionisation potential should enable hole injection from gold electrodes and charge transport in OFETs. Bottom-gate/top-contact field-effect transistors based on zone-cast $C_8$-C-inin films were fabricated and measured at different times to monitor changes in hole mobility and threshold voltage. The first transfer characteristics were measured shortly (1–5 days) after the initial film deposition and again 9 months later for both a rough film, for which polymorph transformation occurred (see Fig. 6a), and for a smooth film, where no conversion of the thin-film polymorph was observed (Fig. 6b).

Both fresh films showed low hole mobilities of up to $\mu_{sat}$ = 0.01 $cm^2 V^{-1} s^{-1}$ in the saturation regime. Determining hole mobilities in the linear regime was not possible due to large bias-stress instabilities when only small drain voltages were applied. Large and mostly irreversible negative shifts of the threshold voltage occurred during those measurements (see ESI,† Fig. S30). The irreversible shift of the threshold voltage might be caused by the irreversible secondary oxidation step of $C_8$-C-inin molecules (to $C_8$-C-inin$^{2+}$) as indicated by cyclic voltammery (see ESI,† Fig. S13). Permanently trapped positive charges in the semiconducting layer could lead to such large threshold voltage shifts.

The charge transport properties of the zone-cast $C_8$-C-inin thin films changed over the course of 9 months depending on their morphology and polymorph stability. For rough films with polymorph transformation, a strong reduction in the drain current on/off ratio was observed, the hole mobility dropped below 0.001 $cm^2 V^{-1} s^{-1}$, and the onset voltage shifted to more

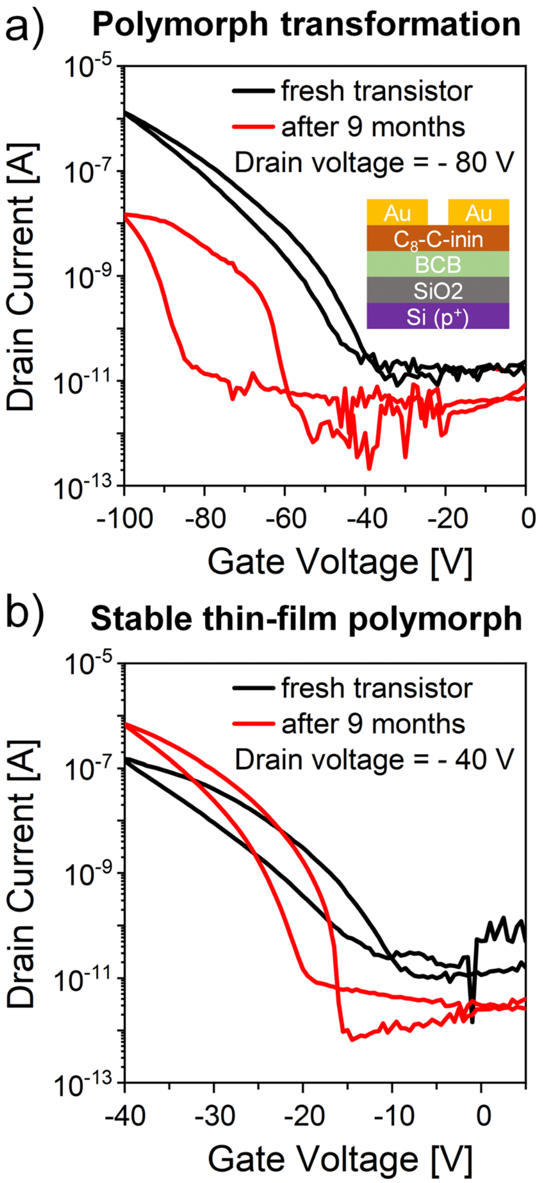

Fig. 6 Transfer characteristics (saturation regime) of OFETs with different zone-cast $C_8$-C-inin films measured shortly (1–5 days) after film deposition and 9 months later. (a) Metastable $C_8$-C-inin film showing polymorph transformation ($V_{ds}$ = −80 V) including schematic transistor layout. (b) Stable $C_8$-C-inin film without polymorph transformation ($V_{ds}$ = −40 V).

negative voltages. This degradation might be explained by differences in the transfer integrals for the changed molecular packing orders. Furthermore, the presence of many different crystal orientations in the transformed polymorph as well as phase boundaries between transformed and metastable polymorphs (see ESI,† Fig. S23) are likely to contribute to charge trapping and overall reduced charge carrier mobilities.

In stark contrast to these devices, the hole mobilities of OFETs with thin smooth films of zone-cast $C_8$-C-inin, which showed no polymorph transformation, actually increased by an order of magnitude (up to $\mu_{sat} = 0.1$ cm$^2$ V$^{-1}$ s$^{-1}$) after aging for 9 months. A steeper subthreshold swing also indicates a lower density of trap states. This enhanced performance might be due to the high molecular mobility of $C_8$-C-inin molecules at crystal edges and defects as discussed above, which may facilitate healing of trap-states through equilibration of the molecular orientations at grain boundaries. It also confirms that the observed device degradation for rough films was not the result of any chemical changes of the $C_8$-C-inin molecules.

In summary, the stabilization of the $C_8$-C-inin thin-film polymorph in highly ordered and smooth zone-cast films not only prevents device degradation due to polymorph transformation but even enhances charge transport after long-term storage in contrast to many other organic semiconductors.

## 3. Conclusion

Thin films of $C_8$-C-inin, a new derivative of 5,10-dihydroindolo[3,2-*b*]indole, were prepared by thermal evaporation and zone-casting from solution, resulting in distinct morphologies. Both types of films exhibited a metastable polymorph that transforms at room temperature and over different time scales into a thermodynamically more stable polymorph. Rough and polycrystalline films with packing defects and grain boundaries (such as those obtained through thermal evaporation) promote and accelerate the large molecular reorientations required for this transformation. Conversely, reducing the density of packing defects through optimized film deposition *via* zone-casting prolongs the time necessary for polymorph transformation from hours to several months or longer. As an enantiotropic polymorphic system with a polymorph transition temperature not far from room temperature, annealing $C_8$-C-inin films does not lead to faster polymorph transitions. Instead, it provides thermodynamic stabilisation of the metastable polymorph and thus a reversal of the polymorph transformation. This example of the small-molecule organic semiconductor $C_8$-C-inin demonstrates that long-term stability of a metastable polymorph and thus the retention of electronic and optical properties can be achieved by controlling the initial film morphology while annealing can provide an additional pathway to metastable polymorphs. Similar effects can be expected for other organic polymorphic systems.

## 4. Experimental methods

### 4.1. Materials

$C_8$-C-inin was synthesized and purified as described in the ESI.† All chemicals were obtained from commercial sources (Sigma Aldrich, Alfa Aesar, Fluorochem, Fisher Scientific, *etc.*) and used without further purification. Dow Cyclotene 3022-35 resin from micro resist technology GmbH was used as the precursor for the crosslinked B-staged divinylsiloxanebenzocyclobutene (BCB) layer.

### 4.2. Zone-cast films

Alkali-free glass substrates (AF32eco, Schott AG, 2 cm × 2.5 cm, thickness 500 μm) and substrates of p-doped silicon (2 cm × 2.5 cm, thickness 500 μm) with and without thermally grown oxide (300 nm $SiO_2$) were cleaned by sonication in acetone and 2-propanol followed by rinsing with deionized water. A diluted solution of BCB precursor in mesitylene (volume 4 : 1) was spin-coated onto the substrates at 4000 rpm in dry nitrogen atmosphere followed by annealing at 290 °C for 1 minute to complete crosslinking. The resulting BCB layer had a thickness of ~100 nm (on glass substrates) or 65 nm (on Si/$SiO_2$ substrates). The $C_8$-C-inin layer was zone-cast using a home-built zone-casting setup as described previously.[4,49] A solution of 0.25 or 2.5 mg $mL^{-1}$ $C_8$-C-inin in toluene, a nozzle and solution temperature of 60 °C, a stage temperature of 80 °C and a casting speed of 0.1 mm $s^{-1}$ were applied, which yielded aligned $C_8$-C-inin films with a thickness of 15–150 nm.

### 4.3. OFET device fabrication

Thermal evaporation of 30 nm thick gold source/drain electrodes through a shadow mask (channel width 1500 μm, channel lengths 40–150 μm) on Si/$SiO_2$/BCB substrates with $C_8$-C-inin thin films completed bottom-gate/top-contact field-effect transistors. To reduce gate leakage, the $C_8$-C-inin films were patterned by mechanically removing the semiconductor around the individual transistor structures.

### 4.4. Thermally evaporated films

Quartz substrates and substrates of silicon with thermally grown $SiO_2$ (300 nm) were soaked in acid mixture (HCl/$HNO_3$) for 24 hours, then washed with water and sonicated in isopropanol, followed by ozone cleaning for 20 mins. Homogeneous thin films of $C_8$-C-inin were thermally evaporated in vacuum at a rate of 0.2 Å $s^{-1}$ using a thermal evaporator (Angstrom Engineering Inc.). The thickness of the films was 80 nm for optical measurements and thin film XRD but 20 nm for AFM measurements.

### 4.5. Characterization

**Thin film XRD.** X-ray diffraction data were collected using Cu-Kα (λ = 1.541 Å) radiation on a Bruker D8 ADVANCE X-ray diffractometer in Bragg–Brentano Geometry equipped with a high-resolution energy dispersive Lynxeye XE detector. Interplanar distances were calculated using Bragg's law $n\lambda = 2d_{khl}\sin(\theta_{hkl})$, where $\theta_{hkl}$ – Bragg angle, $d_{khl}$ – interplanar distance, $\lambda$ – wavelength, and $n$ – order of reflection.

**Grazing incidence wide-angle X-ray scattering (GIWAXS).** GIWAXS measurements of zone-cast films were performed at the BL11 NCD-SWEET beamline at ALBA Synchrotron Radiation Facility (Spain). The incident X-ray beam energy was set to 12.4 keV using a channel cut Si (111) monochromator. The angle of incidence was set between 0.1° and 0.15° to ensure surface sensitivity. The scattering patterns were recorded using a Rayonix LX255-HS area detector. Data are expressed as a function of the scattering vector ($q$), which was calibrated using $Cr_2O_3$ as standard sample, obtaining a sample-to-detector distance of 194.5 mm. 2D GIWAXS patterns were corrected as a function of the components of $q$. 2D GIWAXS patterns of BCB coated silicon substrates were used for background substraction after applying a weighting factor of 0.5.

GIWAXS measurements of thermally evaporated films were carried out on a Xeuss 2.0 instrument equipped with an Excillium MetalJet liquid gallium X-ray source. Films prepared on glass were collected for 900 s using collimating slits of 0.5 × 0.6 mm ("high flux" mode). Alignment was performed *via* three iterative height ($z$) and rocking curve ($\Omega$) scans, with the final grazing incidence angle set to $\Omega = 0.3°$. Scattering patterns were recorded on a vertically-offset Pilatus 1M detector with a sample to detector distance of 385 mm, calibrated using a silver behenate standard to achieve a $q$-range of 0.035–2.0 $Å^{-1}$. Data reduction was performed using the instrument-specific Foxtrot software.

Unit cell sizes and lattice parameters were obtained from GIWAXS data using the MatLab script GIWAXS-SIIRkit provided by Savikhin *et al.*[50] GIWAXS-SIIRkit allows calculating lattice parameters from a GIWAXS pattern by fitting well-defined and oriented diffraction peaks.

**Atomic force micrographs.** Atomic force micrographs of zone-cast $C_8$-C-inin films were recorded using a Bruker Dimension Icon atomic force microscope (AFM) in ScanAsyst™ mode under ambient conditions. Images were processed with Gwyddion 2.6. For thermally evaporated $C_8$-C-inin films, Peak Force – Quantitative Nanomechanical Mapping (PF-QNM) in air was used for imaging, maintaining a modulation frequency of 2 kHz and a peak force value no greater than 500 pN. Bruker™ SNL AFM probes were used for imaging. Imaging was performed with Nanoscope 9.2 software. Nanoscope Analysis 1.8 and MATLAB 2017a were used for data analysis.

**Raman spectroscopy.** Raman spectra were recorded with a Renishaw InVia-Reflex confocal Raman microscope in back-scattering configuration with a 785 nm excitation laser. For each sample, 21 to 64 spectra (50 accumulations) were collected from equally spaced spots over areas of 225 to 1225 $\mu m^2$. Spectra were averaged, smoothed and baseline corrected by subtracting a reference spectrum of a clean substrate without $C_8$-C-inin and an exponential decay background to correct for remaining intensity from scattered laser light.

**Absorption spectroscopy.** UV-vis absorption spectra of zone-cast films and single-crystal powder placed on a cleaned glass substrate were acquired with an Agilent Cary 6000i UV-Vis-NIR absorption spectrometer with a linear transmittance setup. A small aperture was placed in front of the sample for film measurements to select a uniform film area. Measurements of a $C_8$-C-inin solution in hexane (5.5 μmol $L^{-1}$) were carried out with a 1 cm cuvette. Absorption spectra of thermally evaporated films were measured using an Agilent Technologies Cary 60 Spectrometer with a linear transmittance setup.

**Photoluminescence spectroscopy.** Photoluminescence spectra of a dilute $C_8$-C-inin solution in hexane (5.5 μmol $L^{-1}$), of a zone-cast $C_8$-C-inin film, and of single-crystal powder on a cleaned glass substrate were acquired with a Horiba Scientific Fluorolog-3 spectrometer. Photoluminescence spectra of thermally evaporated $C_8$-C-inin film were measured using Jobin Yvon Horiba Fluoromax4 (equipped with xenon arc lamp) or Agilent Technologies Cary Eclipse Fluorescence (equipped with xenon flash lamp) spectrofluorometers.

**Electrical characterization.** Output and transfer characteristics of OFETs were recorded in air with a 4155C Agilent semiconductor parameter analyzer. The overall areal capacitance $C_i$ of the $SiO_2$/

BCB bilayer dielectric layer was estimated to be 8.66 nF·cm$^{-2}$. Field-effect mobilities in the saturation regime ($\mu_{\mathrm{sat}}$) were calculated based on the gradual channel approximation: $\mu_{\mathrm{sat}} = \frac{2L}{WC_{\mathrm{i}}}\left(\frac{\partial\sqrt{I_{\mathrm{d}}}}{\partial V_{\mathrm{gs}}}\right)$, where $L$ – channel length, $W$ – channel width, $V_{\mathrm{gs}}$ – gate-source voltage, and $I_{\mathrm{d}}$ – drain current.

## Author contributions

N. J. H. carried out all experiments if not otherwise mentioned, analysed the data and wrote the manuscript. O. K. synthesized the molecule $C_8$-C-inin, analysed the molecular material properties, performed experiments on thermally evaporated films and co-wrote the manuscript. N. P. T. performed initial experiments of zone-casting $C_8$-C-inin. G. E. M. recorded AFM images of thermally evaporated films. X. R.-M. contributed GIWAXS-measurements of zone-cast films. D. T. contributed GIWAXS-measurements of thermally evaporated films. C. R. performed single-crystal X-Ray crystallography and thin-film XRD measurements of thermally evaporated films. A. I. supervised the synthesis aspects of the project. J. Z. and J. C. conceived and supervised the project and co-wrote the manuscript.

## Conflicts of interest

There are no conflicts to declare.

## Data availability

Data for this article is available on HeiData, the data repository of the University of Heidelberg, at **https://doi.org/10.11588/DATA/C5KIML**.

Crystallographic data for $C_8$-C-inin single-crystal polymorphs 1 and 2 have been deposited at the CCDC under CCDC 2448535 and 2448536.

## Acknowledgements

This research was funded by the Deutsche Forschungsgemeinschaft (DFG) *via* the Collaborative Research Center ‘‘N-Heteropolycycles as Functional Materials’’ SFB 1249/3 projects C06 and C09. X.R.-M. acknowledges funding from the Alexander von Humboldt Foundation. X.R.-M. acknowledges experimental support from staff at the NCD-SWEET beamline at ALBA Synchrotron (experiment ID AV-2023087673). J.C., O.K. and G.E.M. acknowledge the Grantham Centre for Sustainable Futures for PhD funding and EPSRC for research and equipment funding (EP/T012455/1, EP/L022613/1 and EP/R042802/1).

## References

1 H. Chung and Y. Diao, *J. Mater. Chem. C*, 2016, **4**, 3915–3933.
2 F. Würthner, C. R. Saha-Möller, B. Fimmel, S. Ogi, P. Leowanawat and D. Schmidt, *Chem. Rev.*, 2016, **116**, 962–1052.
3 D. W. Davies, G. Graziano, C. Hwang, S. K. Park, W. Liu, D. Yuan, S. C. B. Mannsfeld, S. G. Wang, Y.-S. Chen, D. L. Gray, X. Zhu and Y. Diao, *Cryst. Growth Des.*, 2023, **23**, 719–728.
4 N. J. Herrmann, N. von Coelln, R. M. Teichgreber, S. Höfener, C. Huck, F. Ghalami, S. Settele, M. Hertzog, M. Elstner, P. Tegeder, E. M. Herzig and J. Zaumseil, *J. Mater. Chem. C*, 2023, **11**, 10185–10197.
5 T. Matsukawa, M. Yoshimura, K. Sasai, M. Uchiyama, M. Yamagishi, Y. Tominari, Y. Takahashi, J. Takeya, Y. Kitaoka, Y. Mori and T. Sasaki, *J. Cryst. Growth*, 2010, **312**, 310–313.
6 L. Huang, Q. Liao, Q. Shi, H. Fu, J. Ma and J. Yao, *J. Mater. Chem.*, 2010, **20**, 159–166.
7 C. C. Mattheus, A. B. Dros, J. Baas, G. T. Oostergetel, A. Meetsma, J. L. De Boer and T. T. M. Palstra, *Synth. Met.*, 2003, **138**, 475–481.
8 C. Cocchi, T. Breuer, G. Witte and C. Draxl, *Phys. Chem. Chem. Phys.*, 2018, **20**, 29724–29736.
9 X. Wang, T. Garcia, S. Monaco, B. Schatschneider and N. Marom, *CrystEngComm*, 2016, **18**, 7353–7362.
10 F. Marin, S. Tombolesi, T. Salzillo, O. Yaffe and L. Maini, *J. Mater. Chem. C*, 2022, **10**, 8089–8100.
11 J. A. Schneider, H. Black, H.-P. Lin and D. F. Perepichka, *Chem. Phys. Chem.*, 2015, **16**, 1173–1178.
12 X. Jiao, S. Maniam, S. J. Langford and C. R. Mcneill, *Phys. Rev. Mater.*, 2019, **3**, 013606.
13 M. W. Kim, S. Kwon, J. Kim, C. Lee, I. Park, J. H. Shim, I. S. Jeong, Y. R. Jo, B. Park, J. H. Lee, K. Lee and B. J. Kim, *Small*, 2020, **16**, 1906109.
14 S. Marina, M. Dyson, X. Rodríguez-Martínez, O. G. Reid, R. Li, G. Rumbles, D. Smilgies, A. Amassian, M. Campoy-Quiles, N. Stingelin and J. Martín, *J. Mater. Chem. C*, 2024, **12**, 2410–2415.
15 S. Marina, A. D. Scaccabarozzi, E. Gutierrez-Fernandez, E. Solano, A. Khirbat, L. Ciammaruchi, A. Iturrospe, A. Balzer, L. Yu, E. Gabirondo, X. Monnier, H. Sardon, T. D. Anthopoulos, M. Caironi, M. Campoy-Quiles, C. Müller, D. Cangialosi, N. Stingelin and J. Martin, *Adv. Funct. Mater.*, 2021, **31**, 2103784.
16 A. Brillante, I. Bilotti, R. G. Della Valle, E. Venuti and A. Girlando, *CrystEngComm*, 2008, **10**, 937.
17 J. Socci, T. Salzillo, R. G. Della Valle, E. Venuti and A. Brillante, *Solid State Sci.*, 2017, **71**, 146–151.
18 C.-T. Hsieh, C.-Y. Chen, H.-Y. Lin, C.-J. Yang, T.-J. Chen, K.-Y. Wu and C.-L. Wang, *J. Phys. Chem. C*, 2018, **122**, 16242–16248.
19 P. Yu, Y. Zhen, H. Dong and W. Hu, *Chem*, 2019, **5**, 2814–2853.
20 G. E. Purdum, N. G. Telesz, K. Jarolimek, S. M. Ryno, T. Gessner, N. C. Davy, A. J. Petty, Y. Zhen, Y. Shu, A. Facchetti, G. E. Collis, W. Hu, C. Wu, J. E. Anthony, R. T. Weitz, C. Risko and Y.-L. Loo, *J. Am. Chem. Soc.*, 2018, **140**, 7519–7525.
21 M. R. Caira, *Design of Organic Solids*, Springer, Berlin Heidelberg, 1998, pp. 163–208, DOI: **10.1007/3-540-69178-2_5**.

22 T. Salzillo, A. Campos, A. Babuji, R. Santiago, S. T. Bromley, C. Ocal, E. Barrena, R. Jouclas, C. Ruzie, G. Schweicher, Y. H. Geerts and M. Mas-Torrent, *Adv. Funct. Mater.*, 2020, **30**, 2006115.

23 D. W. Davies, S. K. Park, P. Kafle, H. Chung, D. Yuan, J. W. Strzalka, S. C. B. Mannsfeld, S. G. Wang, Y.-S. Chen, D. L. Gray, X. Zhu and Y. Diao, *Chem. Mater.*, 2021, **33**, 2466–2477.

24 H. Chung, S. Chen, B. Patel, G. Garbay, Y. H. Geerts and Y. Diao, *Cryst. Growth Des.*, 2020, **20**, 1646–1654.

25 L. Catalano, R. Sharma, D. P. Karothu, M. Saccone, O. Elishav, C. Chen, N. Juneja, M. Volpi, R. Jouclas, H.-Y. Chen, J. Liu, G. Liu, E. Gopi, C. Ruzié, N. Klimis, A. R. Kennedy, T. K. Vanderlick, I. Mcculloch, M. T. Ruggiero, P. Naumov, G. Schweicher, O. Yaffe and Y. H. Geerts, *J. Am. Chem. Soc.*, 2024, **146**, 31911–31919.

26 L. Lyu, D. Niu, H. Xie, Y. Zhao, N. Cao, H. Zhang, Y. Zhang, P. Liu and Y. Gao, *Phys. Chem. Chem. Phys.*, 2017, **19**, 1669–1676.

27 D. Paul and J. John, *Chem. – Asian J.*, 2022, **17**, e202200460.

28 I. Cho, S. K. Park, B. Kang, J. W. Chung, J. H. Kim, K. Cho and S. Y. Park, *Adv. Funct. Mater.*, 2016, **26**, 2966–2973.

29 X. Wang, H. Wang, C. Li, L. Qiu, Y. Liu, L. Li and X. Wan, *ChemistrySelect*, 2019, **4**, 5918–5924.

30 A. Fatima, A. Farhat, R. Saleem, R. A. Khera, S. Iqbal and J. Iqbal, *J. Comput. Biophys. Chem.*, 2021, **20**, 71–84.

31 P. V. Santhini, V. Jayadev, S. C. Pradhan, S. Lingamoorthy, P. R. Nitha, M. V. Chaithanya, R. K. Mishra, N. U. KN, J. John and S. Soman, *New J. Chem.*, 2019, **43**, 862–873.

32 Z. R. Owczarczyk, W. A. Braunecker, A. Garcia, R. Larsen, A. M. Nardes, N. Kopidakis, D. S. Ginley and D. C. Olson, *Macromolecules*, 2013, **46**, 1350–1360.

33 J. Hwang, J. Park, Y. J. Kim, Y. H. Ha, C. E. Park, D. S. Chung, S.-K. Kwon and Y.-H. Kim, *Chem. Mater.*, 2017, **29**, 2135–2140.

34 G. S. Lee, H. J. Shin, S. Shome, J. H. Park, S. J. Ko, H. Choi and Y. H. Kim, *Int. J. Energy Res.*, 2021, **45**, 7806–7813.

35 C. H. Ryoo, I. Cho, J. Han, J.-H. Yang, J. E. Kwon, S. Kim, H. Jeong, C. Lee and S. Y. Park, *ACS Appl. Mater. Interfaces*, 2017, **9**, 41413–41420.

36 S. Tongsuk, R. Malatong, T. Unjarern, C. Wongkaew, P. Surawatanawong, T. Sudyoadsuk, V. Promarak and N. Ruangsupapichat, *J. Lumin.*, 2021, **238**, 118287.

37 Y. Y. Jing, Y. Yang, N. Li, Z. Ye, X. Wang, X. Cao and C. Yang, *Luminescence*, 2024, **39**, e4624.

38 T. Unjarern, C. Kaiyasuan, S. Arunlimsawat, P. Surawatanawong, T. Chantarojsiri, T. Sudyoadsuk, V. Promarak and N. Ruangsupapichat, *Org. Electron.*, 2023, **120**, 106848.

39 H. Chung, S. Chen, N. Sengar, D. W. Davies, G. Garbay, Y. H. Geerts, P. Clancy and Y. Diao, *Chem. Mater.*, 2019, **31**, 9115–9126.

40 L. Qiu, X. Wang, N. Zhao, S. Xu, Z. An, X. Zhuang, Z. Lan, L. Wen and X. Wan, *J. Org. Chem.*, 2014, **79**, 11339–11348.

41 N. J. Hestand and F. C. Spano, *Chem. Rev.*, 2018, **118**, 7069–7163.

42 J. Gierschner, L. Lüer, B. Milián-Medina, D. Oelkrug and H.-J. Egelhaaf, *J. Phys. Chem. Lett.*, 2013, **4**, 2686–2697.

43 J. Gierschner and S. Y. Park, *J. Mater. Chem. C*, 2013, **1**, 5818–5832.

44 J. W. Ward, K. P. Goetz, A. Obaid, M. M. Payne, P. J. Diemer, C. S. Day, J. E. Anthony and O. D. Jurchescu, *Appl. Phys. Lett.*, 2014, **105**, 083305.

45 J. Anwar and D. Zahn, *Adv. Drug Delivery Rev.*, 2017, **117**, 47–70.

46 H. Ito, M. Muromoto, S. Kurenuma, S. Ishizaka, N. Kitamura, H. Sato and T. Seki, *Nat. Commun.*, 2013, **4**, 2009.

47 Y. V. Mnyukh, *Mol. Cryst. Liq. Cryst.*, 1979, **52**, 163–199.

48 Y. V. Mnyukh and N. A. Panfilova, *J. Phys. Chem. Solids*, 1973, **34**, 159–170.

49 F. Paulus, J. U. Engelhart, P. E. Hopkinson, C. Schimpf, A. Leineweber, H. Sirringhaus, Y. Vaynzof and U. H. F. Bunz, *J. Mater. Chem. C*, 2016, **4**, 1194–1200.

50 V. Savikhin, H.-G. Steinruck, R.-Z. Liang, B. A. Collins, S. D. Oosterhout, P. M. Beaujuge and M. F. Toney, *J. Appl. Crystallogr.*, 2020, **53**, 1108–1129.